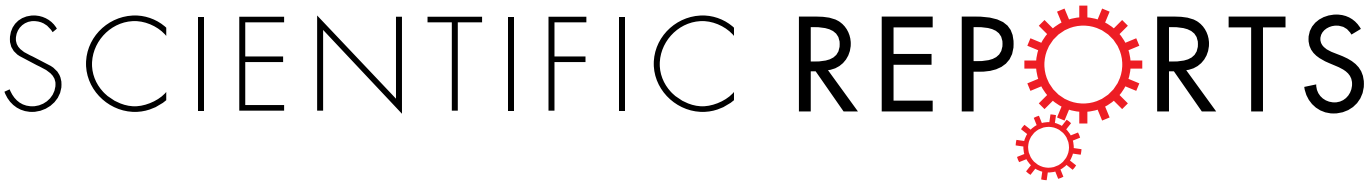

OPEN

Electrochemical properties of novel FeV_2O_4 as an anode for Na-ion batteries

Received: 8 February 2018
Accepted: 23 May 2018
Published online: 11 June 2018

Irish Valerie B. Maggay[1], Lyn Marie Z. De Juan[2], Jeng-Shin Lu[1], Mai Thanh Nguyen[2], Tetsu Yonezawa[2], Ting-Shan Chan[3] & Wei-Ren Liu[1]

Spinel based transition metal oxide – FeV_2O_4 is applied as a novel anode for sodium-ion battery. The electrochemical tests indicate that FeV_2O_4 is generally controlled by pseudo-capacitive process. Using cost-effective and eco-friendly aqueous based binders, Sodium-Carboxymethylcellulose/Styrene butadiene rubber, a highly stable capacity of ~97 mAh·g^{-1} is obtained after 200 cycles. This is attributed to the strong hydrogen bonding of carboxyl and hydroxyl groups indicating superior binding with the active material and current collector which is confirmed by the *ex-situ* cross-section images of the electrode. Meanwhile, only ~27 mAh·g^{-1} is provided by the electrode using poly(vinylidene difluoride) due to severe detachment of the electrode material from the Cu foil after 200 cycles. The obtained results provide an insight into the possible applications of FeV_2O_4 as an anode material and the use of water-based binders to obtain highly stable electrochemical tests for sodium-ion battery.

The commercialization of Lithium ion batteries (LIBs) by Sony in 1991, paved the way for the development of portable devices[1]. However, the excessive costs and geographical constraints of lithium resources, made it impossible for LIBs to sustain and meet the growing demands of rechargeable batteries[2–12]. As a result, alternative battery systems are being explored. One of the most notable systems is the Sodium ion batteries (SIBs) owing to its abundance, low cost and availability[8,11,13–15]. Na atom is larger and heavier than Li atom (1.02 Å vs. 0.76 Å)[16,17]; therefore, the gravimetric and volumetric energy densities of SIBs are generally lower than LIBs. Nevertheless, energy density would not pose a great issue in terms of large-scale energy storage systems[9,12,18]. Numerous progresses on SIBs greatly focus on cathode materials, and although there is a growing number of studies on anode materials, most studies are limited to hard carbons[19–21]. Hard carbon, a non-graphitic carbonaceous compound, is given the highest considerations due to its large interlayer distance disorder structure[3,22]. Pyrolized glucose derived hard carbon prepared by Stevens and Dahn delivered a reversible sodium capacity of 300 mAh·g^{-1} [22,23] However, non-graphitic carbonaceous compounds suffer from high irreversible capacity loss and low capacity retention[22]. Na-alloying type anodes, such as Sn, Sb, P, Ge and In have also been reported to deliver high reversible capacities[22,24,25]. Howbeit, these materials suffer from large volume change during electrochemical tests which results in electrode pulverization, loss of contact with the current collector, and subsequent capacity fading[24,26].

Transition metal oxides (TMOs) have been greatly studied on LIBs due to their high theoretical capacities (>600 mAh·g^{-1}) which is obtained through conversion reaction of oxides with Li[12,21,27–30]. The reduction of metal ions during the lithiation process leads to higher capacities than the commercial graphite anode (in LIBs)[21]. Furthermore, in conversion based anode materials, the anode materials are converted and new phases are expected to form[13]. TMOs can store energy through the conversion of the metals (reduction and oxidation), as well as alloying and de-alloying, which provides high reversibility. Ternary TMOs are known to provide higher electronic conductivities than simple metal oxides[31]. The first conversion anode material for SIBs was introduced by Alcantara's group[32]. When they discharged the battery from 4.1 to 0.0 V, it delivered an initial capacity ~350 mAh·g^{-1} and subsequently decreased to ~250 mAh·g^{-1} at 0.2 V after four cycles. It is generally lower than that of LIBs, but in comparison to hard and soft carbon, $NiCo_2O_4$ still provided a higher capacity.

[1]Department of Chemical Engineering, Chung Yuan Christian University, Taoyuan City, Chungli, 32023, Taiwan. [2]Division of Materials Science and Engineering, Faculty of Engineering, Hokkaido University Kita 13 Nishi 8, Kita-ku, Sapporo, Hokkaido, 060-8628, Japan. [3]National Synchrotron Radiation Research Center (NSRRC), 30076, Hsinchu, Taiwan. Irish Valerie B. Maggay, Lyn Marie Z. De Juan and Jeng-Shin Lu contributed equally to this work. Correspondence and requests for materials should be addressed to W.-R.L. (email: WRLiu1203@gmail.com)

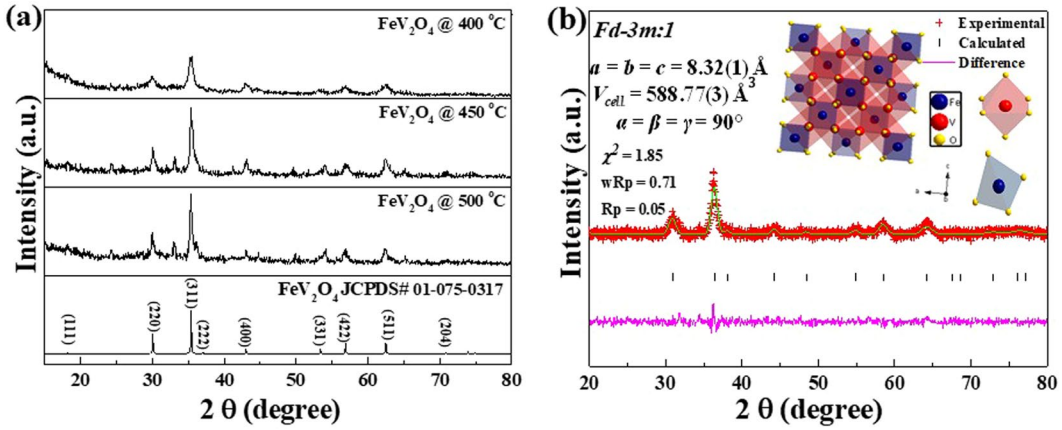

Figure 1. (**a**) XRD profiles of FeV_2O_4 calcined at different temperatures under H_2/N_2 atmosphere and (**b**) Rietveld refinement. Insets: crystal structure of FeV_2O_4 with the FeO_4 and VO_6 polyhedra.

Vanadium metal takes multiform valence states which can provide series of transition metal vanadium-based compounds ($A_xV_yB_z$) (A=Co, Cr, Fe, Zn, Mn, Mg, Bi, etc., B=O, S or Se)[33]. These vanadium-based compounds have been widely used as electrodes for rechargeable batteries for more than 30 years[34]. In LIB systems, numerous vanadium containing compounds have been studied such as, ZnV_2O_4[35,36], CoV_2O_6[37], CuV_2O_6[38], $Cu_{2.33}V_4O_{11}$[39], $FeVO_4$[33,40] and so forth. However, several of these compounds have not been yet applied to Na-ion battery systems. It is known that at 1.0 V, it can achieve multi-electron transfer due to its multivalent properties, indicating a possibility of higher capacity delivery than Ti-based anodes[34,41]. Iron-based materials are known to provide high theoretical capacity due to its multi-valence states (Fe^0, Fe^{2+}, and Fe^{3+}) which provide redox pairs of Fe^0/Fe^{2+}, Fe_0/Fe^{3+} and Fe^{2+}/Fe^{3+}. Furthermore, iron is a highly abundant element with a comparable price to commercial activated carbon, hence making it economically viable for industrial-scale applications[42]. With these advantages provided by iron and vanadium oxides, Fe-V-O compound is expected to exhibit notable electrochemical performance for SIBs applications. Based on these ideas, spinel oxide FeV_2O_4 was prepared and its electrochemical performance was analyzed in this study. The magnetic, orbital and structure phase transitions of FeV_2O_4[43–45] have been widely investigated but it has not been employed as an anode material for both Li and Na-ion battery systems.

The effects of different binders were also carried out in this study. Various studies have used Poly(vinylidene difluoride) (PVdF) as binder for both LIBs and SIBs[6,13,30,46]. In LIBs, PVdF is known to have good electrochemical stability, strong binding ability to both the electrode and current collector, and could absorb electrolyte that facilitates Li^+ transport to the surface of the active materials[46–52]. However, it requires a toxic and expensive solvent (N-methyl-I-1-pyrrolidone, NMP) as its dispersing medium. Furthermore, PVdF is wettable in non-aqueous liquid electrolyte which could lead to the detachment of the electrode from the current collector, thus increasing contact resistance[46]. As for its application in SIBs, it has been reported that PVdF suffers from defluorination during sodium intercalation because of the lack of passivation in Na-ion cell[53].

Na-carboxylmethylcellulose (CMC), a linear polymeric derivative of cellulose with different levels of carboxylmethyl substitution, is one of the aqueous binders that is considered to replace PVdF[47]. Another known water-based binder is the Styrene butadiene rubber (SBR) which possesses higher flexibility, stronger binder force, and better heat resistance than PVdF[54]. Zhang *et al*. reported that the synergistic effect of CMC/SBR offered enhanced rate capability and increased cycling stability for $ZnFe_2O_4$ anode for LIBs. Furthermore, the cross-sectional SEM images of their electrodes revealed the poor contact of the PVdF based electrode with the current collector after cycling. Also, Wang and colleagues claimed improved electrochemical performance of their MoS_2 using CMC/SBR in comparison to PVdF[54]. It is believed that the improved electrochemical properties is due to the high tolerance of water-based polymer binders (such as CMC/SBR) against internal mechanical stress caused by volume expansion[47]. Based on these, this study focuses on the (*i*) preparation of a novel anode material FeV_2O_4 and (*ii*) preliminary analyses of its electrochemical properties for Na – battery systems with the incorporation of non-aqueous (PVdF) and aqueous (CMC/SBR) binders.

Results and Discussion

The XRD profiles of FeV_2O_4 with different calcination temperatures (400–500 °C) are illustrated in Fig. 1(a). It was evident that the spinel structure of FeV_2O_4 are formed when the samples are calcined at 400 °C and all the diffraction peaks are well indexed to the standard diffraction pattern (JCPDS # 01-075-0317). Meanwhile, when the temperature was raised to 450–500 °C, impurity peaks situated at ~25°, 33° appeared which are attributable to V_2O_3 impurity (JCPDS # 00-001-1293). As a result, the sample calcined at 400 °C was used in the electrochemical tests. Rietveld refinement of FVO is shown in Fig. 1(b). FeV_2O_4 crystallizes in a face-centered cubic spinel structure with space group *Fd* $\bar{3}$*m:1*. The lattice parameters were determined to be a = 8.32(1) Å, b = 8.32(1) Å, c = 8.32(1) Å and $\alpha = \beta = \gamma = 90°$ with a cell volume of 588.77(3) $Å^3$. The error bar of the lattice parameters and cell volume are depicted in Supplementary Fig. S1. The calculated average of the lattice parameters is 8.338 ± 0.027 Å with an average cell volume of 588.563 ± 0.291 $Å^3$, respectively. Lastly, the calculated crystallite

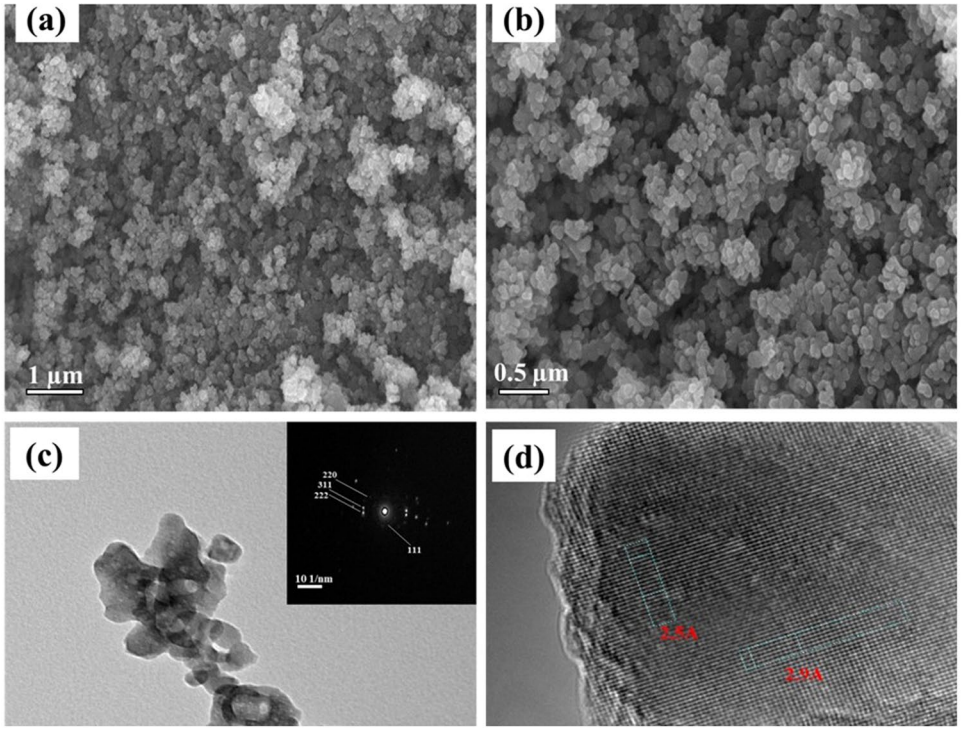

Figure 2. (**a**,**b**) SEM, (**c**) TEM and inset: SAED, and (**d**) HRTEM images of FeV_2O_4.

size of FeV_2O_4 at 400 °C is 88.461 Å. The crystal structure and the corresponding coordination environments of Fe^{2+} and V^{3+} ions are displayed in the insets of Fig. 1(b). Iron cations are positioned in the tetrahedral (FeO_4) 8a sites, while vanadium ions are situated in the octahedral (VO_6) 16d sites and a network or grid of corner-sharing tetrahedra with cubic-closed pack oxygen anions reside in the 32e sites[55]. To further prove the crystallinity of FeV_2O_4 post heat-treated at 400 °C, a slower scan rate of 0.02 °·s^{-1} was used to test its XRD. Based on Fig. S2, all peaks were indexed to the standard XRD patterns and no impurity was detected.

The morphologies and elemental compositions of FeV_2O_4 are depicted in Fig. 2(a–d). It was evident from the SEM images in Fig. 2(a,b) that FeV_2O_4 are agglomerated with irregular shapes. This is further confirmed by the TEM image in Fig. 2(c). The SAED in the inset of Fig. 2(c) confirms the crystallinity of FeV_2O_4 as it agrees with the characteristic diffraction peaks. HRTEM image of FeV_2O_4 in Fig. 2(d) show the lattice fringes of 2.9 Å and 2.5 Å which correspond to the (220) and (311) planes of FeV_2O_4, respectively. The elemental composition of FeV_2O_4 was confirmed using EDS technique as shown in Fig. S2a. The characterization was executed four times at different sites to confirm even distributions of Fe, V and O. In Fig. S2b the bar graph of the atomic % of the elements are displayed with the average compositions, corresponding standard deviations of the elements and errror bars. Based on the gathered data, the calculated $At.\%_{AVE}$ composition (Fe:V:O) = 14.35:27.3:58.35 is close to the stoichiometric ratio of FeV_2O_4 demonstrating uniform distribution of the elements. In addition, the elemental mapping in Fig. S3 further validates the composition and even distribution of the elements.

The wide scan in Fig. 3(a) shows all the possible elements presented in the sample primarily: Iron (Fe), Vanadium (V) and Oxygen (O). Meanwhile Fig. 3(b–d) illustrates the deconvoluted narrow scans of Fe, V and O to confirm the oxidation states of each elements. Figure 3(b) reveal the existence of Fe^{2+} (FeO) as indicated by the Fe $2p_{3/2}$ and Fe $2p_{1/2}$ peaks at 709.76 eV and 722.96 eV, respectively. The pink line located at 716.5 eV was due to the satellite peak of Fe^{2+} and the spin-orbit splitting between $2p_{3/2}$ and $2p_{1/2}$ were both calculated to be 13.2 eV which concurs with the standard value of 13.1 eV. Meanwhile, both V^{3+} and V^{5+} are found to co-exist as presented in Fig. 3(c). The peaks corresponding to V $2p_{3/2}$ and V $2p_{1/2}$ are situated at 515.48 eV and 523.08 eV, respectively for V^{3+}. On the other hand, V^{5+} ions have peaks situated at 516.48 eV for V $2p_{3/2}$ and 524.184 eV for V $2p_{1/2}$. The calculated spin-orbit splitting for V $2p_{3/2}$ and V $2p_{1/2}$ for both V^{3+} and V^{5+} are 7.6 eV and 7.7 eV, respectively which are in agreement with the standard value of 7.64 eV[4]. The pink line at ~ 520 eV is a satellite peak that could be attributed to the existence of both $V^{3+/5+}$. The ratio of V^{3+}:V^{5+} was calculated to be 3:2. The presence of V^{5+} could be attributed to slight the surface oxidation[56]. Lastly, Fig. 3d displays the XPS of O1s. The deconvoluted peaks at 530.12 eV and 529.22 eV were attributed to the metal oxides of FeO, V_2O_3 and V_2O_5.

Due to the surface oxidation of the sample, X-ray absorption near edge structure (XANES) spectrum of V K-edge were determined to probe the local oxidation of Vanadium. Supplementary Fig. S4 compares the K-edge XANES profile of V in FeV_2O_4 with standard metallic vanadium and vanadium oxides. The spectra in Fig. S4a display pre-edge, low-energy shoulder and edge energy absorption peaks. The pre-edge peaks correspond to the coordination environment of V in which the peak intensity is inversely proportional to the coordination geometries[57]. It is assigned as the forbidden transition $1s \rightarrow 3d$ followed by a low-energy shoulder peak which is attributed to the $1s \rightarrow 4p$. Finally, the strong peak corresponds to the dipole-allowed transition $1s \rightarrow 4p$[57]. It can be

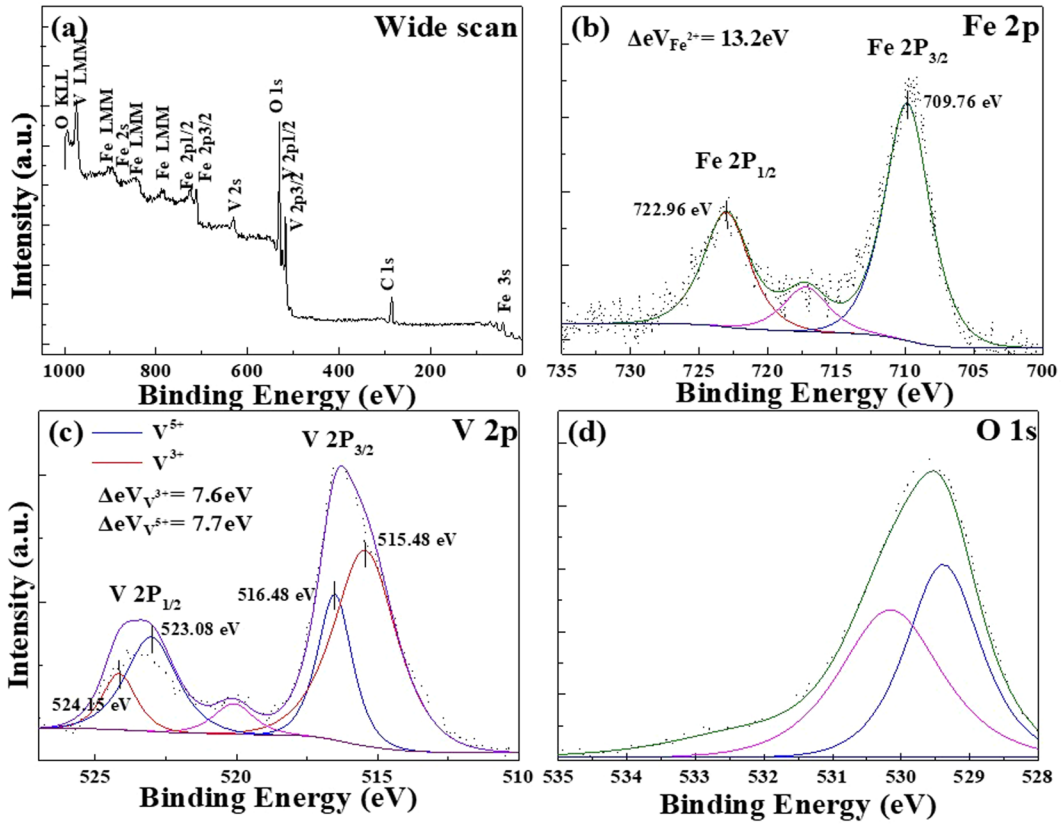

Figure 3. XPS of FeV_2O_4: (**a**) Wide scan and narrow scans of (**b**) Fe, (**c**) V, and (**c**) O.

observed that V_2O_5 and VO_2 have more defined and intense peaks compared to V_2O_3 and FeV_2O_4. According to Nabavi and colleagues[58], V^{5+} in V_2O_5 has both VO_4 and VO_5 coordination states whereas the V in standard V_2O_3 and FeV_2O_4 both occupy an octahedral site (VO_6). Unlike V_2O_5, both standard V_2O_3 and FeV_2O_4 do not have a shoulder peak prior to the edge-energy absorption peak. In Fig. S4b, it can be clearly discerned that the edge energies ($1s \rightarrow 4p$) of different vanadium oxides shift to higher energies. This energy shift is known as chemical shift which follows the Kunzl's and is linearly proportional to the valence of the absorbing vanadium atoms[57]. The inset in Fig. S4b shows the comparison of the pre-edge and edge energy peaks of FeV_2O_4 with the standard V_2O_3 and V_2O_5. Although the pre-edge peaks of V_2O_3 and V_2O_5 are both located at the same peak, the intensity of V_2O_5 is higher because of its VO_4 and VO_5 polyhedra. On the other hand, the first energy edge peaks of FeV_2O_4 and V_2O_3 are close to each other. Moreover, V K-edge spectra profiles of FeV_2O_4 and V_2O_3 are qualitatively similar, thus confirming the successful synthesis of FeV_2O_4 with V^{3+} oxidation state.

The electrochemical evaluation of $Na/NaClO_4$(EC:DEC)/FeV_2O_4 are evaluated and exhibited in Fig. 4. The galvanostatic charge/discharge of FeV_2O_4 using PVdF and CMC/SBR (FVO-PVdf and FVO-CMC/SBR) as binders are represented in Fig. 4(a,b). Although the intital charge/discharge profiles (at 100 $mA{\cdot}g^{-1}$) of the two electrodes look similar, the capacity of FVO-PVdF electrode was two times higher than FVO-CMC/SBR (333 $mAh.g^{-1}$ vs. 167 $mAh.g^{-1}$). However, the coulombic efficiencies were 40% and 56% for FVO-PVdF and FVO-CMC/SBR, respectively. The irreversible capacity was due to the formation of solid electrolyte interphase (SEI) layer between the anode and the electrolyte which is caused by the decomposition of the solvent in the electrolyte[14]. After prolonged cycling at 200 $mA{\cdot}g^{-1}$, the charge/discharge profiles revealed very poor stability and high voltage offset for PVdF. This was ascribed to the large polarization and mechanical energy dissipation caused by induced stress during the rapid charge and discharge process[59]. On the other hand, the profiles of the FVO-CMC/SBR electrode appear to overlap even after 200 cycles denoting good stability and low polarization.

Cycle tests with corresponding coulombic efficencies of FVO-PVdF and FVO-CMC/SBR are illustrated in Fig. 4(c). The first three cycles for formation were tested at 100 $mAh.g^{-1}$ while the rest were tested at 200 $mA.g^{-1}$. Evidently, the first few cycles of FVO-PVdF was higher than that of FVO-CMC/SBR however, prolonged cycling resulted in rapid capacity fading and lower coulombic efficiency. After 100 cycles, it was only able to retain about 39% of its capacity upon running at 200 $mA.g^{-1}$ with a coulombic efficiency of 99%. Further cycling to 200 cycles caused the battery to die eventually. It is theorized that that rapid charge/discharge caused the PVdF electrode to suffer from cracks, large volume expansion and loss of contact from the current collector. Conversely, the FVO-CMC/SBR depicts a stable cycle test upto 200 cycles. As mentioned above, the inital capacities of FVO-PVdF are higher than FVO-CMC/SBR, however, as the test continued, it was revealed that FVO-CMC/SBR delivered a more stable capacity.

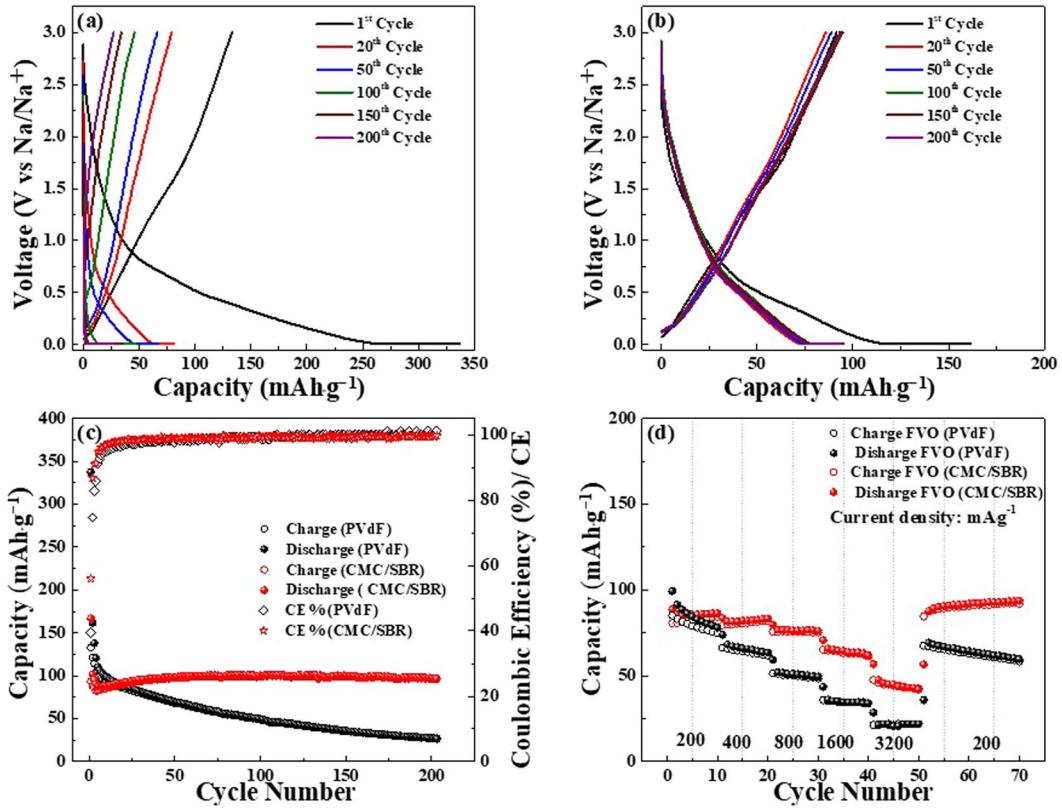

Figure 4. Electrochemical performance of FeV_2O_4 electrodes. Galvanostatic charge/discharge profiles of (**a**) FVO-PVdF and (**b**) FVO-CMC/SBR electrodes at potential window of 0.01–3.0 V. Comparisons of the (**c**) cycle life and (**d**) rate capability tests of FVO-PVdF and FVO-CMC/SBR electrodes.

It was noticeable that there was a gradual increase in the capacity, which is very common in TMOs and has been widely observed in LIBs applications. The capacity increase was due to the formation of reversible pseudo-capacitive polymeric/gel film like that is believed to be responsible for the extra uptake of Li^+ on the SEI layer[60,61]. Since LIBs and SIBs are governed by the same rocking chair mechanism, the electrochemical properties of TMOs in SIBs are also affected by this phenomena. Moreover, since the morphology of the FeV_2O_4 is highly agglomerated, there are inactive sites in the electrode that didn't form an initial reaction in the sodiation and desodiation process. With continued cycle test, nano-sized particles are believed to have formed which eventually became exposed and provided more active sites during the sodiation and desodiation process. After 200 cycles, FVO-CMC/SBR obtained a reversible capacity of ~97 $mAh.g^{-1}$ with a coulombic efficiency of 99%. At this stage, CMC/SBR was able to overcome the large volume expansion and maintained a good contact with the Cu foil. Even though FVO-CMC/SBR provided a highly stable capacity, it is obvious that the delivered capacities were very low. The theoretical capacity of FeV_2O_4 is believed to be ~967 $mAh{\cdot}g^{-1}$ (1 C) considering 8 mol of Na^+ during full conversion process. However, at 100 $mA{\cdot}g^{-1}$ only 1.4 mol of Na^+. This huge difference could be attributed to the follwing factors: large ionic radius of Na atom, thicker SEI layer (effect of electrolyte, which is not a scope of this research), and few active sites for Na^+ to induce full conversion of the Fe and V metals. In order to achieve improved electrochemical properties of FeV_2O_4, futher developments should be done such as carbon coating to buffer volume expansion, metallic doping to increase kinetics, controlling its morphology, or providing a layered structure. And while these methods could provide increased capacity, the stability of the electrode is hugely affected by the binder.

Aside from the cycle tests, rate capability of the two electrodes were also studied and is shown in Fig. 4(d). FVO-PVdF electrode has average discharge capacities of 85, 66, 52, 36, and 22 $mAh{\cdot}g^{-1}$ at current densities of 200, 400, 800, 1600, and 3200 $mA.g^{-1}$, respectively. When cycled back to 200 $mA{\cdot}g^{-1}$, it was able to recover an average capacity of 63 $mAh{\cdot}g^{-1}$, which is 25% less of the initial discharge cycle. Meanwhile, FVO-CMC/SBR electrode delivered an average discharge capacities of 86, 82, 77, 65, and 46 at 200, 400, 800, 1600, and 3200 $mA{\cdot}g^{-1}$, respectively. Upon cycling back to 200 $mA{\cdot}g^{-1}$, it recovered an average of 90 $mAh{\cdot}g^{-1}$ which is higher than the former average at 200 $mA{\cdot}g^{-1}$. These results are all indicative of the better stability that CMC/SBR offer over prolonged cycle test.

As mentioned above, it was inferred that FVO-PVdF electrode suffer from huge cracks on the surface and detachment from the Cu foil. To have further insight on the binding abilities of the different binders, *ex-situ* SEM analyses of the electrodes were performed. Supplementary Fig. S5 show the surface and cross-section morphologies of FVO-PVdF. The pristine electrode in Fig. S5a displayed uniform coating, however, it appears to have some shallow cracks which could have been formed upon drying the electrode. After the initial charge/discharge cycle

(Fig. S5b), huge and deep cracks are seen on the surface and the distances between the cracks range from 1.72–7.29 µm. However, the effect of continued cycle, caused the particles to become interconnected and the cracks on the surface were lessened. Furthermore, the cross-section images were also studied as shown in Fig. S5(d–g). The pristine electrode has an average thickness (D_{ave}) of 11.32 µm. After one cycle, expansion is evident, and the D_{ave} increased to 15.88 µm and the electrode was evidently detached from the current collector resulting in increased contact resistance. Further sodiation and desodiation, caused the electrode material to be severely detached from the Cu foil as shown in the low magnification image of the electrode in Fig. S5f. Also, cracks at the bottom of the electrode were present. The average thickness after 200 cycles was calculated to be 34.14 µm (Fig. S5g), indicating huge expansion by ~201%. The inevitable huge volume expansion, detachment from the current collector and cracks are attributable to the weak hydrogen bonding of fluorine in PVdF (Fig. S7a) with the active material and current collector[54,62].

In comparison, supplementary Fig. S6 displays the *ex-situ* surface and cross-section morphologies of FVO-CMC/SBR. In Fig. S6a, the pristine electrode does not have obvious cracks on the surface and shows uniform coating. The carboxyl chains in CMC (Fig. S7b) provides an effective surface charge on the FeV_2O_4 and Super-P particles, therefore stabilizing the particles dispersion through an electrostatic double-layer repulsion mechanism[54,63]. After one cycle, cracks were also present on the surface as shown in Fig. S6b. However, comparing it to the cracks on FVO-PVdF electrode, the cracks appear to be shallow and short. In fact, the gaps were measured to be from 0.74–2.79 µm which are extremely smaller than that of FVO-PVdF electrode. Similarly, the surface of the electrode in Fig. S6c, appear to become denser and the particles are more connected as a result of the SEI formation on the surface and the swelling of the binder[54]. Some of the initial small pores as seen in Fig. S6a, were almost gone and the surface appeared to be smoother and more compact. In contrast to the FVO-PVdF after 200 cycles, FVO-CMC/SBR has no evident cracks on the surface. The cross-sections of the electrodes were also analyzed. The average thickness of the pristine electrode in Fig. S6d is measured to be 11.93 µm and after one charge and discharge cycle, (Fig. S6e), the D_{ave} increased to 14.04 µm. Fig. S6(f) shows the cross-section of the electrode cycled up to 200 cycles with $D_{ave} = 22.40$ µm, denoting 88% expansion. Huge cracks were also present, but the electrode material was still strongly attached to the Cu foil. Nevertheless, it is 2x lower than the volume expansion provided by PVdF. The relatively stronger adhesion of CMC/SBR on the current collector could be ascribed to the strong hydrogen bond of the carboxyl and hydroxyl groups in CMC with the FeV_2O_4, Super-P and Cu foil[54,62]. Zhang *et al.* noted that CMC makes the electrode extremely stiff and brittle when used alone as a binder. It easily forms cracks and can make the electrode slide-off the current collector. Combining CMC with SBR lessens the brittleness of the electrode. In comparison to PVdF, CMC/SBR provide smaller Young's modulus, larger maximum elongation, and improved adhesion to the current collector[54,64].

The plateaus in the galvanostatic charge/discharge profiles of FVO-CMC/SBR which correspond to the reduction and oxidation of Fe and V are not very distinct which is very common for other TMOs applied for both LIBs and SIBs[12,15,65–67]. Cyclic voltammetry test (CV) provides confirmation of the conversion of the metals. The CV profile of FVO-CMC/SBR is shown in Supplementary Fig. S8. It displays CV curves at a constant scan rate of 0.1 $mV{\cdot}s^{-1}$. During the first cycle, there are two broad reduction peaks located at ~0.3–0.6 V and ~1.0–1.4 V, and a narrow and broad oxidation peaks at 0.05 V and ~1.25–1.75 V, respectively. The oxidation peak at 0.05 V is attributed to Super-P. In the subsequent cycles, the reduction peak at ~0.8–1.4 V disappeared, which implies that it is due to the formation of SEI layer. The broad peak at ~0.3–0.6 V shifted to ~0.6–0.8 V in the 2^{nd}-5^{th} cycles denoting irreversible electrochemical reaction in the initial discharge cycle[68]. Meanwhile, the oxidation peaks at ~1.25–1.75 V is still present in the succeeding cycles. It can be clearly seen that the CV profiles for the subsequent cycles are overlapping each other showing excellent reversibility.

It is speculated that the reduction and oxidation peaks for both Fe and V coincides with each other. In the works of Gao *et al.* on FeO/C[69], they suggested that the reduction of of $Fe^{2+} \rightarrow Fe^0$ occurs at ~0.7 V and a broad oxidation peak at ~ 1.5–2.0 V that corresponds to the oxidation of $Fe^0 \rightarrow Fe^{2+}$. Jiang and colleagues studied V_2O_3 nanowires for LIB and they found out that the reduction of $V^{3+} \rightarrow V^0$ is situated at 0.68 V and the oxidation occurs in two step process ($V^0 \rightarrow V^{3+}$) located at 1.25 and 2.62 V[70]. The reported oxidation and reduction peaks for Fe in LIBs agree with the obtained reduction peak of $Fe^{2+} \rightarrow Fe^0$ at ~0.6–0.8 V, and oxidation peak of $Fe^0 \rightarrow Fe^{2+}$ at ~1.25–1.75 V. However, taking into consideration the strong V-O bonding[34], obtaining metallic V will be difficult. Hence, the low capacity of FeV_2O_4. As mentioned earlier, the CV of Li-V_2O_3 has a broad reduction peak (0.68 V) and two oxidation peaks (1.25 and 2.62 V). Conversely, in the CV of Na-FeV_2O_4, only one oxidation peak is observed. Ergo, the broad reduction peak at ~0.6–0.8 V corresponds to $V^{3+} \rightarrow V^{2+}$ and the broad oxidation peak ca. 1.25–1.75 V denotes $V^{2+} \rightarrow V^{3+}$. The CV profile of SIBs are broader than LIBs due to the larger size, heavier mass and slower mobility of Na^+ than Li^+[66].

In order to understand the capacitive behavior of FeV_2O_4, CV measurements at different scan rates were performed (Fig. 5(a)). As expected, the CV curves tend to deviate from its original position as the scan rate is increased which is due to the increase in polarization and ohmic resistance. The relationship between the current and the scan rate was determined using the equaiton[14]:

$$i = av^b \tag{1}$$

where the i is the measured current and v is the scan rate. The b-value can be calculated using the slope of $\log(v)$ vs. $\log(i)$. If the b-value is close to 0.5, the electrochemical behavior is controlled by diffusion process, on the other hand, if the b-value is close to 1.0, it is based on capacitive process. Figure 5(b) illustrates the linear relationship of $\log(v)$-$\log(i)$ using different scan rates and based on the fitting, the obtained cathodic and anodic b-value were calculated to 0.75 and 1.08, respectively. These values confirm the electrochemical behavior of FeV_2O_4 was mainly due to pseudo-capacitive process, hence a higly stable cycle test is obtained[14,71–73].

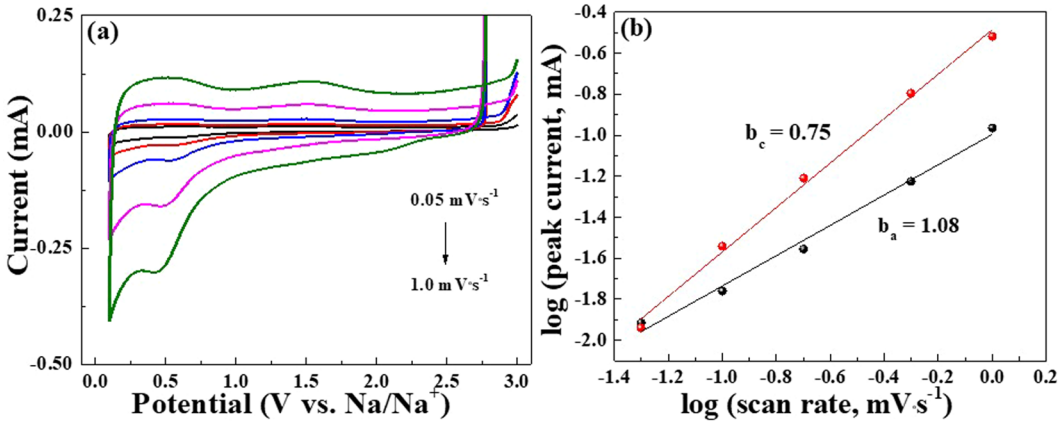

Figure 5. (**a**) CV curves of FVO-CMC/SBR with different scan rates from 0.05 to 1.0 mV·s^{-1} from 0.01–3.0 V. (**b**) Graph of log(v) vs. log(i).

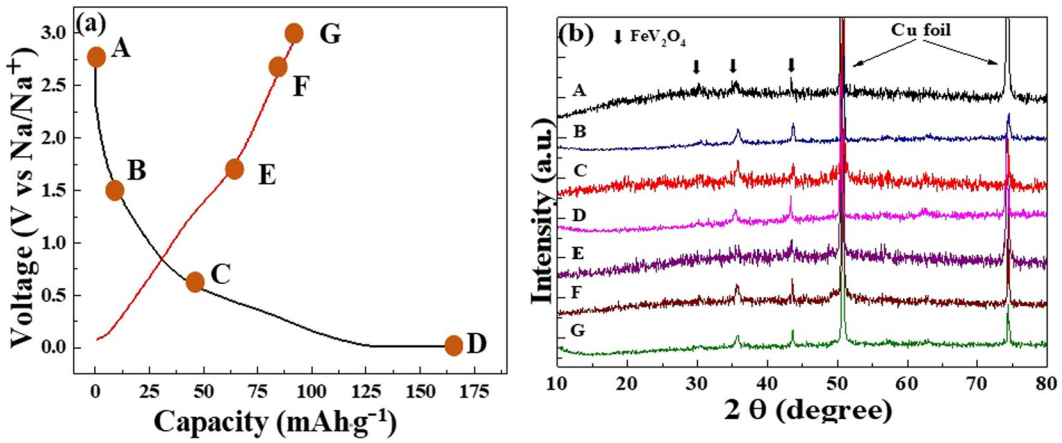

Figure 6. (**a**) Galvanostatic charge/discharge profile of FVO-CMC/SBR electrodes with orange marks corresponding to different depths of charge and discharge and (**b**) *Ex-situ* XRD profiles as indicated by the orange marks (A = pristine; B = D1.5 V, C = D0.5 V, D = D0.01 V and E = C1.5 V, F = C2.8 V and G = C3.0 V).

To get a better understanding of the mechanism that governs conversion materials such as FeV_2O_4 in SIBs, it is necessary to perform *ex-situ* analyses. For TMOs, it is essential to recognize the conversion reaction that transpires during sodiation and desodiation or if there have been occurance of any phase transformations. It was mentioned that in full conversion, FVO could achieve ~967 mAh·g^{-1}, however based on the gathered data, full conversion of the metals were not obtained. Consequently, the reaction mechanism is as follows:

$$FeV_2O_4 + 2xNa^+ + 2xe^- \leftrightarrow Fe + 2VO + 2xNa_2O(0 < x < 1) \quad (2)$$

To further verify whether full conversion of the metals or any phase transformations have transpired during sodiation and desodiaion, *ex-situ* XRD characterizations of FVO-CMC/SBR electrodes were implemented. Figure 6b shows the six electrodes which were charged and discharged at certain voltages based on the CV profiles and galvanostatic charge/discharge profiles (Fig. 6(a)). The fresh electrode has the crystalline peaks of the spinel compound. When discharged and charged to different voltages, it is obvious that the XRD peaks indexed to FeV_2O_4 are still present indicating incomplete conversion reaction. It implies that incomplete conversion reaction occurred during sodiation and desodiation resulting in low capacities. This phenomenon is comparable to the works of Zhou *et al.*[67] on $NiFe_2O_4$ and Mai *et al.*[74] on $NaAlTi_3O_8$ in which their *in-situ* XRD did not indicate any conversion of the metals. However, in Fig. 6b, there is a subtle shift of the XRD peaks to the lower angle when discharged to 0.01 V. This occurance demonstrates lattice expansion due to the insertion of Na^+ upon sodiation. Subsequently, when charged to 1.5–3.0 V, the XRD peaks indexed to FeV_2O_4 shifted to the right indicating release of Na^+ upon desodiation[74]. It is also speculated that the thick SEI layer could have played a huge part on this. Hence, only few active sites were exposed to Na^+ during sodiation.

The conversion reaction mechanism of metal oxides are not yet fully understood in Na-ion systems. Further characterizations of the electrodes using *in-situ* XRD sychrotron or *in-situ* Neutron diffraction analyses must be employed since these equipment are more highly sensitive to light elements such as Na and O[74]. Nevertheless,

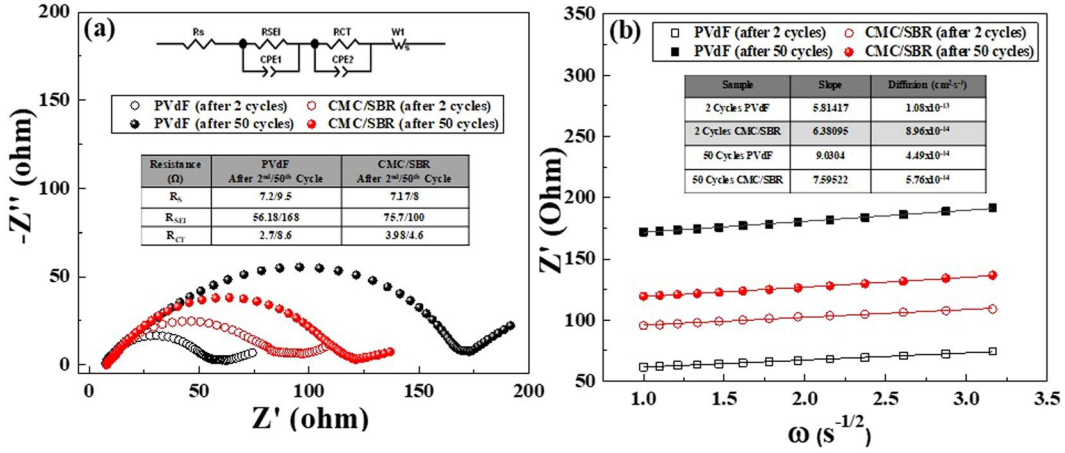

Figure 7. (**a**) EIS and (**b**) diffusion coefficient calculations of FVO-PVdF and -CMC/SBR electrodes.

FeV_2O_4 electrode has a very high stability and reversibility which is ascribed to its pseudo-capacitive properties with the aid of the exceptional properties of CMC and SBR.

Using Electrochemical Impedance Spectroscopy (EIS), the internal resistance in the coin cell were determined and calculated. Figure 7(a) shows a typical EIS profile which is comprised of semicircles and a straight sloping line at a lower frequency region[75]. The semicircle found in the highest frequency is denoted as R_S and is generally known as the electrolyte resistance. The semicircle in the middle frequency is ascribed to R_{CT} and R_{SEI} which correspond to charge transfer resistance and SEI film resistance, respectively. The sloping line, W or Warburg impedance located at the lower frequency represents the Na^+ diffusion. The insets in Fig. 7(a) display the equivalent circuit and the calculated R_S, R_{SEI}, and R_{CT} of FVO-PVDF and -CMC/SBR after 2 and 50 cycles. The calculated R_S, R_{SEI}, and R_{CT} of FVO-PVdF electrde were 7.2, 56.18 and 2.7 Ω, after 2 cycles and increased to 9.5, 168, and 8.6, respectively after 50 cycles. On the other hand, FVO-CMC/SBR provided R_S, R_{SEI}, and R_{CT} of 7.17, 75.7 and 3.98 Ω, respectively after 2 cycles. The resistance increased to 8, 100 and 4.6 Ω for R_S, R_{SEI}, and R_{CT}, respectively after the 50th discharge cycle. The large R_{SEI} for both electrodes verify the poor initial coulombic efficiencies and incomplete conversion of the metals which is highly affected by the electrolyte. Comparing the two electrodes, the initial R_{SEI} and R_{CT} of FVO-PVdF is lower than FVO-CMC/SBR which is in agreement with the initial higher capacity delivered by FVO-PVdF electrode. However, after 50 cycles of (dis)charge cycles, the internal resistance of FVO-PVdF became siginificantly higher compared to FVO-CMC/SBR. These stipulate that PVdF failed to overcome the loss of contact between the active material and Cu foil and the large volume expansion that has arose during the sodiation and desodiation process hence, the large internal resistance. Moreover, it further proves that the fluorine atoms in PVdF only form weak hydrogen bonds with the active material and current collector[54]. The kinetics of the diffusion species were also investigated and calculated using the formula[76]:

$$\sigma = \frac{RT}{n^2F^2A\sqrt{2}}\left(\frac{1}{C_{Li}D_{Li}^{0.5}}\right) \quad (3)$$

where R is the ideal gas constant, T is temperature in Kelvin, F is the Faraday's constant, A is the electrode surface, C_{Li} is the concentration of Li in the electrolyte, and D_{Li} is the diffusion coefficient By calculating the slope (σ), from EIS, D_{Li} were calculated to be 8.965×10^{-14} and 5.762×10^{-14} $cm^2 \cdot s^{-1}$ for FVO-CMC/SBR and 1.08×10^{-13} and 4.49×10^{-14} $cm^2 \cdot s^{-1}$ for FVO-PVdF after the 2nd and 50th cycle, respectively. Initially, the Na^+ diffusion for FVO-PVdF is slightly faster than FVO-CMC/SBR. After 50 cycles, there was a considerable decrease on the diffusion of Na^+ ions in FVO-PVdF electrode. On the other hand, a very subtle decrease in the diffusion kinetics of FVO-CMC/SBR was observed. In fact, the increase in the internal resistance of the cell and the decrease in kinetics are very minimal even after 50 cycles. These agree with the trend in the cycle life tests in which after 50 cycles (FVO-CMC/SBR), it was able to retain 100 $mAh \cdot g^{-1}$ with a very high stability suggesting that FeV_2O_4 could be viable conversion anode material for Na-ion battery. Although the obtained capacities were relatively low, it is believed that modifying its morphology and framework, doping with metals, and coating with carbon could highly improve its overall performance.

Conclusions

Spinel oxide-FeV_2O_4 was employed as a novel anode material for sodium-ion battery. It was verified that its electrochemical behavior is mainly governed by pseudo-capacitive process. Incomplete conversion reaction was discovered in the *ex-situ* XRD. This could be due to the presence of inactive sites in the electrode, formation of thick SEI layer since no additives were used in the electrolyte and the strong V-O bonding. By using CMC and SBR as binders, a highly stable cycle test was achieved compared to PVdF. This was ascribed to the strong hydrogen bonds formed between the carboxyl/hydroxyl groups in CMC with the active material and Cu foil. Moreover, SBR provided better adhesion of the slurry to the Cu foil. Although FVO-CMC/SBR only provided a reversible capacity of ~97 $mAh \cdot g^{-1}$ at 200 $mA \cdot g^{-1}$ for 200 cycles, this study provided preliminary investigations on the application of FeV_2O_4 as a conversion based anode material for sodium-ion battery.

Methods

Materials synthesis. Pure-phase FeV_2O_4 were obtained through simple solvothermal synthesis. 1.2120 g of Iron nitrate nonahydrate ($Fe(NO_3)_2{\cdot}9H_2O$), 0.7019 g of Ammonium vanadate, (NH_4VO_3) were mixed in 40 mL Methanol under vigorous stirring at room temperature with the subsequent addition of 0.2521 g of Oxalic acid monohydrate. The mixture was then transferred to a 100 mL Teflon-lined stainless-steel autoclave and kept in an oven at 200 °C for 24 hours. The obtained powder was then washed repeatedly with Ethanol and Acetone and dried overnight. Finally, the precipitates were calcined at 400–500 °C for 4 hours under H_2/N_2 reducing atmosphere to ensure the formation of spinel compounds.

Characterization. The crystallinity of the samples was characterized using X-ray diffractometer with Cu Kα ($\lambda = 1.5418$ Å) generated at 45 kV and 30 mA. The data were gathered in the 2θ range of 10° to 80° with a scan rate of $0.05°{\cdot}sec^{-1}$. XRD data were analyzed using General Structure Analysis System (GSAS) software to obtain Rietveld Refinement. The elemental compositions were analyzed through X-ray Photoelectron Spectroscopy (XPS, JEOL Photoelectron Spectrometer (ESCA), JPS-9200, monochromatic Al-Kα), V K-edge X-ray absorption spectra (XAS conducted at National Synchrotron Radiation Research Center (NSRRC), Hsinchu, Taiwan using BL01C1 and BL17C1 beamlines) and Energy Dispersive X-ray Spectroscopy (EDS, X-MAX). The morphology and elemental mapping and crystal structure of the samples were analyzed via tunneling electron microscope Cs-corrected Scanning Transmission Electron Microscope (FEI-Titan3 G2-60-300 operating at 200 kV and scanning electron microscope (SEM) – Hitachi S-4100. For *ex-situ* XRD characterizations, the batteries were opened after designated charge and discharge voltages inside an Ar-gas filled glove box with with H_2O and O_2 content <0.5 ppm. The anode electrodes were carefully collected, washed with dimethyl carbonate (DMC) to remove the electrolyte and were vacuumed overnight to remove excess solvents.

Electrochemical Measurement. The electrochemical performances of the batteries were measured by assembling CR2032 coin cells. Two slurries were prepared with similar compositions of 70:15:15 for active material (FeV_2O_4), Super-P (Carbon black, 40 nm), and binder. For aqueous based binder, 9 wt.% of CMC ($Mw = 2 \times 10^5$ Da) and 6 wt. % of SBR was dissolved in DI H_2O. Meanwhile, 15 wt. % of PVdF ($Mw = 1 \times 10^6$ Da) was dissolved in NMP. The prepared slurries were coated onto 10 μm copper foil which was used as the working electrode of the battery. The samples were punched (14 mm) and dried at 120 °C for 8 h in vacuum system to remove the residual solvents. The batteries were assembled in an Ar-gas filled glove box with H_2O and O_2 content <0.5 ppm using sodium disks as the counter electrode, 1 M of $NaClO_4$ in ethylene carbonate (EC) and diethyl carbonate (DEC) (1:1 in volume ratio) as electrolyte, and glass fiber filter disks as the separators. The discharge/charge tests were analysed using AcuTech System in the voltage range of 0.01 V and 3.0 V at room temperature constant voltage charge process. The mass loading of these sample is in the range of 2.60 ± 0.30 mg/cm^2. The cyclic voltammograms (CV) were measured by CH Instruments Analyzer CHI 6273E at a scan rate of $0.1\ mV{\cdot}s^{-1}$ between 0.01 V and 3.0 V and the Electrochemical Impedance of the samples were tested in the frequency range from 0.01-100000 Hz. For the *ex-situ* analyses, the electrodes were opened inside an Ar-gas filled glove box with H_2O and O_2 content <0.5 ppm. The electrodes were washed with dimethyl carbonate (DMC) to remove excess electrolytes and were dried inside the vacuum chamber overnight to prevent oxidation.

References

1. Kim, S. W., Seo, D. H., Ma, X., Ceder, G. & Kang, K. Electrode materials for rechargeable sodium-ion batteries: potential alternatives to current lithium-ion batteries. *Adv. Energy Mater.* **2**, 710–721 (2012).
2. Qu, B. *et al*. Layered SnS2-Reduced Graphene Oxide Composite–A High-Capacity, High-Rate, and Long-Cycle Life Sodium-Ion Battery Anode Material. *Adv. Mater.* **26**, 3854–3859 (2014).
3. Slater, M. D., Kim, D., Lee, E. & Johnson, C. S. Sodium-ion batteries. *Adv. Funct. Mater.* **23**, 947–958 (2013).
4. Zheng, C., Zeng, L., Wang, M., Zheng, H. & Wei, M. Synthesis of hierarchical ZnV_2O_4 microspheres and its electrochemical properties. *CrystEngComm* **16**, 10309–10313 (2014).
5. Kaliyappan, K., Liu, J., Lushington, A., Li, R. & Sun, X. Highly Stable $Na_{2/3}(Mn_{0.54}Ni_{0.13}Co_{0.13})\ O_2$ Cathode Modified by Atomic Layer Deposition for Sodium-Ion Batteries. *ChemSusChem* **8**, 2537–2543 (2015).
6. Krengel, M., Adelhelm, P., Klein, F. & Bensch, W. FeV_2S_4 as a high capacity electrode material for sodium-ion batteries. *ChemComm* **51**, 13500–13503 (2015).
7. Jian, Z. *et al*. Superior electrochemical performance and storage mechanism of $Na_3V_2(PO_4)_3$ cathode for room-temperature sodium-ion batteries. *Adv. Energy Mater.* **3**, 156–160 (2013).
8. Xu, Y., Zhu, Y., Liu, Y. & Wang, C. Electrochemical performance of porous carbon/tin composite anodes for sodium-ion and lithium-ion batteries. *Adv. Energy Mater.* **3**, 128–133 (2013).
9. Liu, Q. *et al*. Facile synthesis of $FeSi_4P_4$ and its Sodium Ion Storage Performance. *Electrochim. Acta* **247**, 820–825 (2017).
10. Jiang, X., Liu, H., Song, J., Yin, C. & Xu, H. Hierarchical mesoporous octahedral $K_2Mn_{1-x}Co_xFe(CN)_6$ as a superior cathode material for sodium-ion batteries. *J. Mater. Chem. A* **4**, 16205–16212 (2016).
11. Kim, Y., Ha, K. H., Oh, S. M. & Lee, K. T. High-Capacity Anode Materials for Sodium-Ion Batteries. *Chem. Eur. J.* **20**, 11980–11992 (2014).
12. Liu, Y., Zhang, N., Yu, C., Jiao, L. & Chen, J. $MnFe_2O_4$@C nanofibers as high-performance anode for sodium-ion batteries. *Nano Lett.* **16**, 3321–3328 (2016).
13. Krengel, M. *et al*. CuV_2S_4: A high rate-capacity and stable anode material for sodium-ion batteries. *ACS Appl. Mater. Interfaces* 9, (21283–21291 (2017).
14. Huang, Y. *et al*. Enhancing Sodium-Ion Storage Behaviors in $TiNb_2O_7$ by Mechanical BallMilling. *ACS Appl. Mater. Interfaces* 9, (8696–8703 (2017).
15. Su, D., Dou, S. & Wang, G. Hierarchical Vanadium Pentoxide Spheres as High-Performance Anode Materials for Sodium-Ion Batteries. *ChemSusChem* **8**, 2877–2882 (2015).
16. Kim, S.-O. & Manthiram, A. The facile synthesis and enhanced sodium-storage performance of a chemically bonded CuP_2/C hybrid anode. *ChemComm* **52**, 4337–4340 (2016).
17. Su, H., Jaffer, S. & Yu, H. Transition metal oxides for sodium-ion batteries. *Energy Storage Materials* **5**, 116–131 (2016).
18. Pan, H., Hu, Y.-S. & Chen, L. Room-temperature stationary sodium-ion batteries for large-scale electric energy storage. *Energy Environ. Sci.* **6**, 2338–2360 (2013).

19. Zhu, Y. *et al*. Electrospun Sb/C fibers for a stable and fast sodium-ion battery anode. *ACS nano* **7**, 6378–6386 (2013).
20. Wang, Y., Wang, C., Guo, H., Wang, Y. & Huang, Z. A nitrogen-doped three-dimensional carbon framework for high performance sodium ion batteries. *RSC Adv.* **7**, 1588–1592 (2017).
21. Lee, J.-W., Shin, H.-S., Lee, C.-W. & Jung, K.-N. Carbon-and Binder-Free $NiCo_2O_4$ Nanoneedle Array Electrode for Sodium-Ion Batteries: Electrochemical Performance and Insight into Sodium Storage Reaction. *Nanoscale Res. Lett.* **11**, 45 (2016).
22. Jiang, Y. *et al*. Transition metal oxides for high performance sodium ion battery anodes. *Nano Energy* **5**, 60–66 (2014).
23. Stevens, D. & Dahn, J. High capacity anode materials for rechargeable sodium-ion batteries. *J. Electrochem. Soc.* **147**, 1271–1273 (2000).
24. Luo, W. *et al*. Na-ion battery anodes: materials and electrochemistry. *Acc. Chem. Res.* **49**, 231–240 (2016).
25. Darwiche, A. *et al*. Better cycling performances of bulk Sb in Na-ion batteries compared to Li-ion systems: an unexpected electrochemical mechanism. *J. Am. Chem. Soc.* **134**, 20805–20811 (2012).
26. Chevrier, V. L. & Ceder, G. Challenges for Na-ion negative electrodes. *J. Electrochem. Soc.* **158**, A1011–A1014 (2011).
27. Poizot, P., Laruelle, S., Grugeon, S., Dupont, L. & Tarascon, J. Nano-sized transition-metal oxides as negative-electrode materials for lithium-ion batteries. *Nature* **407**, 496 (2000).
28. Hu, J., Li, H., Huang, X. & Chen, L. Improve the electrochemical performances of Cr_2O_3 anode for lithium ion batteries. *Solid State Ion.* **177**, 2791–2799 (2006).
29. Cabana, J., Monconduit, L., Larcher, D. & Palacin, M. R. Beyond Intercalation-Based Li-Ion Batteries: The State of the Art and Challenges of Electrode Materials Reacting Through Conversion Reactions. *Adv. Mater.* **22** (2010).
30. He, C. *et al*. Carbon-encapsulated Fe_3O_4 nanoparticles as a high-rate lithium ion battery anode material. *ACS nano* **7**, 4459–4469 (2013).
31. Li, Z., Huang, X., Hu, J., Stein, A. & Tang, B. Synthesis and electrochemical performance of three-dimensionally ordered macroporous $CoCr_2O_4$ as an anode material for lithium ion batteries. *Electrochim. Acta* **247**, 1–11 (2017).
32. Alcántara, R., Jaraba, M., Lavela, P. & Tirado, J. $NiCo_2O_4$ spinel: First report on a transition metal oxide for the negative electrode of sodium-ion batteries. *Chem. Mater.* **14**, 2847–2848 (2002).
33. Yan, N., Xu, Y., Li, H. & Chen, W. The preparation of $FeVO_4$ as a new sort of anode material for lithium ion batteries. *Mater. Lett.* **165**, 223–226 (2016).
34. Xu, X. *et al*. Alkaline earth metal vanadates as sodium-ion battery anodes. *Nat. Commun.* **8**, 460 (2017).
35. Zeng, L. *et al*. ZnV_2O_4–CMK nanocomposite as an anode material for rechargeable lithium-ion batteries. *J. Mater. Chem.* **22**, 14284–14288 (2012).
36. Zhu, X. *et al*. Nanophase ZnV_2O_4 as stable and high capacity Li insertion electrode for Li-ion battery. *Curr. Appl. Phys.* **15**, 435–440 (2015).
37. Zhang, L. *et al*. Acetylene black induced heterogeneous growth of macroporous CoV_2O_6 nanosheet for high-rate pseudocapacitive lithium-ion battery anode. *ACS Appl. Mater. Interfaces* **8**, 7139–7146 (2016).
38. Prahasini, P. *et al*. A novel attempt for employing brannerite type copper vanadate as an anode for lithium rechargeable batteries. *J. Mater. Sci. Mater. Electron.* **27**, 3292–3297 (2016).
39. Morcrette, M. *et al*. A reversible copper extrusion-insertion electrode for rechargeable Li batteries. *Nat. Mater.* **2**, 755 (2003).
40. Liu, X., Cao, Y., Zheng, H., Chen, X. & Feng, C. Synthesis and modification of FeVO 4 as novel anode for lithium-ion batteries. *Appl. Surf. Sci.* **394**, 183–189 (2017).
41. Augustyn, V. & Dunn, B. Low-potential lithium-ion reactivity of vanadium oxide aerogels. *Electrochim. Acta* **88**, 530–535 (2013).
42. Yu, S. *et al*. Synthesis and Application of Iron-based Nanomaterials as Anode of Lithium-Ion Batteries and Supercapacitors. J. *Mater. Chem. A*, https://doi.org/10.1039/C8TA01683F (2018).
43. Myoung, B. R., Kim, S. J., Lim, J. T., Kouh, T. & Kim, C. S. Microscopic evidence of magnetic and structure phase transition in multiferroic spinel FeV_2O_4. *AIP Adv.* **7**, 055828 (2017).
44. Wakihara, M., Shimizu, Y. & Katsura, T. Preparation and magnetic properties of the FeV_2O_4 Fe_3O_4 system. *J. Solid State Chem.* **3**, 478–483 (1971).
45. MacDougall, G. *et al*. Magnons and a two-component spin gap in FeV_2O_4. *Phys. Rev. B* **89**, 224404 (2014).
46. Chou, S.-L., Pan, Y., Wang, J.-Z., Liu, H.-K. & Dou, S.-X. Small things make a big difference: binder effects on the performance of Li and Na batteries. *Phys. Chem. Chem. Phys.* **16**, 20347–20359 (2014).
47. Zhang, W., Dahbi, M. & Komaba, S. Polymer binder: a key component in negative electrodes for high-energy Na-ion batteries. *Curr. Opin. Chem. Eng.* **13**, 36–44 (2016).
48. Maleki, H., Deng, G., Kerzhner-Haller, I., Anani, A. & Howard, J. N. Thermal Stability Studies of Binder Materials in Anodes for Lithium-Ion Batteries. *J. Electrochem. Soc.* **147**, 4470–4475 (2000).
49. Li, J., Christensen, L., Obrovac, M., Hewitt, K. & Dahn, J. Effect of heat treatment on Si electrodes using polyvinylidene fluoride binder. *J. Electrochem. Soc.* **155**, A234–A238 (2008).
50. Liu, G. *et al*. Optimization of acetylene black conductive additive and PVDF composition for high-power rechargeable lithium-ion cells. *J. Electrochem. Soc.* **154**, A1129–A1134 (2007).
51. Choi, D. *et al*. Li-ion batteries from $LiFePO_4$ cathode and anatase/graphene composite anode for stationary energy storage. *Electrochem. Commun.* **12**, 378–381 (2010).
52. Fedorková, A. *et al*. PPy doped PEG conducting polymer films synthesized on $LiFePO_4$ particles. *J. Power Sources* **195**, 3907–3912 (2010).
53. Yabuuchi, N., Kubota, K., Dahbi, M. & Komaba, S. Research development on sodium-ion batteries. *Chem. Rev.* **114**, 11636–11682 (2014).
54. Zhang, R. *et al*. Water soluble styrene butadiene rubber and sodium carboxyl methyl cellulose binder for $ZnFe_2O_4$ anode electrodes in lithium ion batteries. *J. Power Sources* **285**, 227–234 (2015).
55. Zhang, Q. *et al*. Ordering process and ferroelectricity in a spinel derived from FeV_2O_4. *Phys. Rev. B* **85**, 054405 (2012).
56. Hager, H., Greiner, S., Heubl, G. & Stahl-Biskup, E. *Hagers Handbuch der Pharmazeutischen Praxis: Drogen PZ Folgeband 2*. (Springer-Verlag, 2013).
57. Wong, J., Lytle, F. W., Messmer, R. P. & Maylotte, D. H. K-edge absorption spectra of selected vanadium compounds. *Phys. Rev. B* **30**, 5596–5610 (1984).
58. Nabavi, M., Sanchez, C. & Livage, J. Structure and properties of amorphous V_2O_5. *Philos. Mag.* **63**, 941–953 (1991).
59. Wang, W., Jiang, B., Hu, L. & Jiao, S. Nasicon material $NaZr_2(PO_4)_3$: a novel storage material for sodium-ion batteries. *J. Mater. Chem. A* **2**, 1341–1345 (2014).
60. Wang, H. *et al*. Cobalt oxide-carbon nanosheet nanoarchitecture as an anode for high-performance lithium-ion battery. *ACS Appl. Mater. Interfaces* **7**, 2882–2890 (2015).
61. Kim, Y. *et al*. Probing the additional capacity and reaction mechanism of the RuO_2 anode in lithium rechargeable batteries. *ChemSusChem* **8**, 2378–2384 (2015).
62. Lee, B.-R. & Oh, E.-S. Effect of molecular weight and degree of substitution of a sodium-carboxymethyl cellulose binder on $Li_4Ti_5O_{12}$ anodic performance. *J. Phys. Chem. C* **117**, 4404–4409 (2013).
63. Lestriez, B., Bahri, S., Sandu, I., Roué, L. & Guyomard, D. On the binding mechanism of CMC in Si negative electrodes for Li-ion batteries. *Electrochem. Commun.* **9**, 2801–2806 (2007).

64. Chong, J. *et al*. A comparative study of polyacrylic acid and poly (vinylidene difluoride) binders for spherical natural graphite/$LiFePO_4$ electrodes and cells. *J. Power Sources* **196**, 7707–7714 (2011).
65. Wang, Y., Huang, H., Xie, Q., Wang, Y. & Qu, B. Rational design of graphene-encapsulated $NiCo_2O_4$ core-shell nanostructures as an anode material for sodium-ion batteries. *J. Alloy. Comp.* **705**, 314–319 (2017).
66. Zhang, N. *et al*. 3D Porous γ-Fe_2O_3@C Nanocomposite as High-Performance Anode Material of Na-Ion Batteries. *Adv. Energy Mater*. **5** (2015).
67. Zhou, K. *et al*. A multi-functional gum arabic binder for $NiFe_2O_4$ nanotube anodes enabling excellent Li/Na-ion storage performance. *J. Mater. Chem. A* **5**, 18138–18147 (2017).
68. Li, J. *et al*. Hollow $MnCo_2O_4$ submicrospheres with multilevel interiors: from mesoporous spheres to yolk-in-double-shell structures. *ACS Appl. Mater. Interfaces* **6**, 24–30 (2013).
69. Gao, M. *et al*. FeO/C anode materials of high capacity and cycle stability for lithium-ion batteries synthesized by carbothermal reduction. *J. Alloy. Comp.* **565**, 97–103 (2013).
70. Jiang, H. *et al*. Ultrafine V_2O_3 nanowire embedded in carbon hybrids with enhanced lithium storage capability. *Ind. Eng. Chem. Res.* **54**, 2960–2965 (2015).
71. Xu, D. *et al*. A Hierarchical N/S-Codoped Carbon Anode Fabricated Facilely from Cellulose/Polyaniline Microspheres for High-Performance Sodium-Ion Batteries. *Adv. Energy Mater*. **6** (2016).
72. Augustyn, V. *et al*. High-rate electrochemical energy storage through Li^+ intercalation pseudocapacitance. *Nat. Mater.* **12**, 518–522 (2013).
73. Zhu, S. *et al*. $NiSe_2$ nanooctahedra as an anode material for high-rate and long-life sodium-ion battery. *ACS Appl. Mater. Interfaces* 9, (311–316 (2016).
74. Ma, X., An, K., Bai, J. & Chen, H. $NaAlTi_3O_8$, A Novel Anode Material for Sodium Ion Battery. *Sci. Rep.* **7**, 162 (2017).
75. Zhang, S., Xu, K. & Jow, T. Electrochemical impedance study on the low temperature of Li-ion batteries. *Electroch. Acta* **49**, 1057–1061 (2004).
76. Ong, T. & Yang, H. Lithium intercalation into mechanically milled natural graphite: electrochemical and kinetic characterization. *J. Electrochem. Soc.* **149**, A1–A8 (2002).

Acknowledgements

This research is supported by the National Science Council of Taiwan under contract numbers: 102-2221-E-033-050-MY2 and 102-3011-P-033-003. It is also partially funded by Hokkaido University, microstructural characterization platform as a program of Nanotechnology Platform of the Ministry of Education, Culture, Sports, Science and Technology (MEXT), Japan.

Author Contributions

W.R.L., T.Y. and M.T.N. supervised the research and contributed editing of manuscript. All authors discussed and commented on the manuscript.

Additional Information

Supplementary information accompanies this paper at https://doi.org/10.1038/s41598-018-27083-z.

Competing Interests: The authors declare no competing interests.

Publisher's note: Springer Nature remains neutral with regard to jurisdictional claims in published maps and institutional affiliations.